Experimental Neurology 367 (2023) 114471

Contents lists available at ScienceDirect

Experimental Neurology

journal homepage: www.elsevier.com/locate/yexnr

Research paper

Cell-specific *Dyt1* ΔGAG knock-in to basal ganglia and cerebellum reveal differential effects on motor behavior and sensorimotor network function

B.J. Wilkes [a,*], R.Z. Adury [a], D. Berryman [b], L.R. Concepcion [a], Y. Liu [b], F. Yokoi [b], C. Maugee [b], Y. Li [b], D.E. Vaillancourt [a,b,c]

[a] Department of Applied Physiology and Kinesiology, University of Florida, Gainesville, FL, USA
[b] Norman Fixel Institute for Neurological Diseases, Department of Neurology, University of Florida, Gainesville, FL, USA
[c] Department of Biomedical Engineering, University of Florida, Gainesville, FL, USA

ARTICLE INFO

Keywords:
dystonia
Dyt1
torsinA
sensorimotor
basal ganglia
dopamine-2 receptor
cerebellum
Purkinje cells
fMRI
functional connectivity
diffusion MRI

ABSTRACT

Dystonia is a neurological movement disorder characterized by repetitive, unintentional movements and disabling postures that result from sustained or intermittent muscle contractions. The basal ganglia and cerebellum have received substantial focus in studying DYT1 dystonia. It remains unclear how cell-specific ΔGAG mutation of torsinA within specific cells of the basal ganglia or cerebellum affects motor performance, somatosensory network connectivity, and microstructure. In order to achieve this goal, we generated two genetically modified mouse models: in model 1 we performed *Dyt1* ΔGAG conditional knock-in (KI) in neurons that express dopamine-2 receptors (D2-KI), and in model 2 we performed *Dyt1* ΔGAG conditional KI in Purkinje cells of the cerebellum (Pcp2-KI). In both of these models, we used functional magnetic resonance imaging (fMRI) to assess sensory-evoked brain activation and resting-state functional connectivity, and diffusion MRI to assess brain microstructure. We found that D2-KI mutant mice had motor deficits, abnormal sensory-evoked brain activation in the somatosensory cortex, as well as increased functional connectivity of the anterior medulla with cortex. In contrast, we found that Pcp2-KI mice had improved motor performance, reduced sensory-evoked brain activation in the striatum and midbrain, as well as reduced functional connectivity of the striatum with the anterior medulla. These findings suggest that (1) D2 cell-specific *Dyt1* ΔGAG mediated torsinA dysfunction in the basal ganglia results in detrimental effects on the sensorimotor network and motor output, and (2) Purkinje cell-specific *Dyt1* ΔGAG mediated torsinA dysfunction in the cerebellum results in compensatory changes in the sensorimotor network that protect against dystonia-like motor deficits.

1. Introduction

Dystonia is a neurological movement disorder characterized by repetitive, unintentional movements and disabling postures stemming from sustained or intermittent muscle contractions (Albanese et al., 2013). Dystonia embodies a number of clinical syndromes, including focal dystonia to specific body parts, or generalized dystonia affecting a majority of the body. Collectively, dystonia represents the third most common movement disorder. The etiology of dystonia can be idiopathic or inherited through known genetic factors. Early-onset generalized DYT1 dystonia is a heterozygous autosomal dominant condition linked to an in-frame ΔGAG mutation of the *TOR1A/DYT1* gene, which causes misfolding of the TorsinA protein, and is the most common genetic type of dystonia (Ozelius et al., 1997).

The basal ganglia and cerebellum have received substantial focus in the study of DYT1 dystonia. A commonly used medication used in people with DYT1 dystonia is trihexyphenidyl, a cholinergic antagonist. Studies have shown that only 60–70% of patients show significant treatment effects from trihexyphenidyl and there can be difficult side effects for patients when on the medication (Burke et al., 1986; Fahn, 1983). Although abnormal cholinergic dynamics are observed in the basal ganglia and cerebellum in association with DYT1 dystonia (Mazere et al., 2021; Xing et al., 2022), a number of studies suggest that non-cholinergic cell types may also play an important role in the pathophysiology of dystonia (Hayashi et al., 2008; Lee et al., 2014; Liu et al., 2020; Maltese et al., 2014; Miyazaki, 2012).

The most consistent structural alterations found in human neuroimaging studies similarly implicate the basal ganglia and cerebellum in

* Corresponding author at: Department of Applied Physiology and Kinesiology, University of Florida, P.O. Box 118205, Gainesville, FL 32611, USA.
E-mail address: bwilkes@ufl.edu (B.J. Wilkes).

https://doi.org/10.1016/j.expneurol.2023.114471
Received 17 February 2023; Received in revised form 8 June 2023; Accepted 12 June 2023
Available online 14 June 2023

dystonia (for a review, see MacIver et al., 2022). Regional brain volume differences in dystonia have primarily been identified in the basal ganglia, whereas studies of white matter with diffusion MRI (dMRI) have revealed reduced integrity in the cerebellothalamocortical tract that correlated with motor network activity (Argyelan et al., 2009; Carbon et al., 2008). Although both nonmanifesting and clinically manifesting DYT1 mutation carriers show these white matter abnormalities proximal to the cerebellum, nonmanifesting mutation carriers have an additional region of white matter tract changes in distal portions of this tract near the thalamus, possibly representing a secondary compensatory change in those without clinically manifesting dystonia (Argyelan et al., 2009).

Research in transgenic animal models has also greatly increased our understanding of torsinA dysfunction. Broadly speaking, *Dyt1* knock-out (KO) models provide insights about reduced levels of endogenous torsinA, whereas *Dyt1* ΔGAG knock-in (KI) models help to understand the effects of mutant torsinA analogous to the protein mutation observed in people with early-onset DYT1 dystonia (Dang et al., 2005; Sharma et al., 2005; Shashidharan et al., 2005). Homozygous models of torsinA dysfunction are nonviable or show neonatal lethality, but heterozygous *Dyt1* KO and KI models may display dystonic postures or subtle motor deficits, paired with other pathophysiological features of dystonia. The *Dyt1* ΔGAG KI mouse model is one of the most widely studied genetic models of dystonia and recapitulates many features of DYT1 dystonia, including motor behavior deficits, abnormal muscle contractions observed with electromyography, and altered brain microstructure (Dang et al., 2005; DeAndrade et al., 2016). Similar to humans with DYT1 dystonia, *Dyt1* ΔGAG KI mice also exhibit microstructural alterations in both basal ganglia and cerebellar circuitry (Song et al., 2014; Song et al., 2013; Uluğ et al., 2011).

Although studying the basal ganglia and cerebellum independently has greatly increased our understanding of mechanisms contributing to the pathophysiology of dystonia, it has been suggested that dystonia may be best viewed as a functional network disorder, where there is disrupted flow and integration of signals across multiple components of the sensorimotor network (Burciu et al., 2017; DeSimone et al., 2017; Simonyan, 2018). Therefore, considering dystonia to be a product of either basal ganglia or cerebellar dysfunction is likely a false conceptual perspective. What is lacking from this perspective is a more comprehensive understanding of how torsinA dysfunction in specific cell types contributes to dystonia-related phenotypes and changes in sensorimotor network pathophysiology and connectivity. Moreover, evaluating the effects of cell-specific torsinA dysfunction in vivo enables assessment of network properties not evident when such components are studied separately, and may provide key insights into the clinical and neurophysiological deficits in dystonia (Hallett, 1995; Martella et al., 2014; Martella et al., 2009; Quartarone and Hallett, 2013).

In this study, we sought to identify the impact of torsinA mutation in specific cells in the basal ganglia or cerebellum and their corresponding effects on network-level connectivity and microstructure. To accomplish this goal, we generated two cell-specific *Dyt1* mouse models. In model 1 neurons that express dopamine-2 receptors have *Dyt1* ΔGAG conditional KI (D2-KI), which include medium spiny neurons of the indirect pathway, striatal cholinergic interneurons, and dopaminergic neurons of the basal ganglia. In model 2, neurons that express Purkinje cell protein-2 have *Dyt1* ΔGAG conditional KI (Pcp2-KI), which include Purkinje cells of the cerebellum. In both of these models, we assessed motor behavior and performed in vivo neuroimaging at ultra-high field (11.1 T). We used functional magnetic resonance imaging (fMRI) to assess sensory-evoked brain activation and connectivity, along with diffusion MRI (dMRI) to assess microstructural changes. The rationale for using in vivo sensory-evoked fMRI is that there is prior clinical and neurophysiological evidence demonstrating somatosensory processing deficits in dystonia patients (Hallett, 1995). In particular, there is evidence thermal sensory processing deficits in patients with focal dystonia (Suttrup et al., 2011) and Dyt1 ΔGAG knock-in mice (Scuteri et al., 2021). Our previous work using this methodology has also demonstrated that it is sensitive to subtle deficits in the sensorimotor network (Chu et al., 2020; Wilkes et al., 2021). We evaluated the microstructure of brain regions in the sensorimotor network with dMRI because this technique has shown promise in studying neurodegeneration in human conditions and animal models (Burciu et al., 2017; Chu et al., 2020; Colon-Perez et al., 2019; DeSimone et al., 2017). We hypothesized that D2-KI mice would show motor deficits and altered sensorimotor network properties, due to the impact on torsinA across multiple cell types in the basal ganglia and the critical role those cell types play in the pathophysiology of dystonia. We hypothesized that Pcp2-KI mice would not have motor deficits but would show compensatory brain changes within the sensorimotor network, as informed by our prior work in the Purkinje cell-specific *Dyt1* KO model (Yokoi et al., 2012; Zhang et al., 2011) and imaging findings in the cerebellothalamic tract that distinguish nonmanifesting and clinically manifesting DYT1 mutation carriers (Argyelan et al., 2009).

2. Materials and methods

2.1. Experimental design

This study included two dystonia mouse models. In both models, *Dyt1* ΔGAG KI was driven by a promoter specific to the cell type that was targeted. In model 1, we targeted neurons of the basal ganglia using the dopamine-2 (*D2*) receptor gene as a promoter (Yokoi et al., 2020) – hereafter referred to as D2-KI. Although D2 receptors exist in other brain regions, in mice the DRD2 BA-Cre mediated recombination is highest in the striatum and low in other brain regions (Gong et al., 2007). In model 2, we targeted cerebellar Purkinje cells using the Purkinje cell protein-2 (*Pcp2*) gene as a promoter (Lyu et al., 2020) – hereafter referred to as Pcp2-KI. Mice from both D2-KI and Pcp2-KI cohorts were generated on the C57BL/6 background strain. We used litter-mate control groups specific to each model to minimize the effects of background strain and cage-to-cage variability on comparisons of mutant versus control animals. The same animals went through each stage of the experiment. First, motor behavior assessments were performed on all animals and included accelerated rotarod and beam-walking tests. Mice were rested for one week between these behavioral tests and for one week before neuroimaging. Next, four types of MRI scans were acquired for every animal: an anatomical scan, sensory-evoked fMRI, resting-state fMRI, and diffusion MRI. Experimenters performing behavioral testing and MRI acquisition were blind to which animals belonged to the experimental or control groups for each model. After all testing and data preprocessing were complete, genotyping was performed, and experimenters were unblinded to enable group-wise comparisons. Methods for each aspect of this study are described in detail in the following sections.

2.2. Animals

All experiments were performed in accordance with the National Institutes of Health guide for the care and use of Laboratory animals (NIH Publications No. 8023, revised 1978). The D2-KI cohort included 29 (19 male, 10 female) mice with heterozygous *Dyt1* ΔGAG conditional knock-in to neurons expressing the dopamine-2 receptor (D2Cre+/− Swap+/−) with mean age 304 ± 34 days, and 30 (20 male, 10 female) control mice (D2Cre+/−) with mean age 294 ± 36 days. The Pcp2-KI cohort included 37 (20 male, 17 female) mice with heterozygous *Dyt1* ΔGAG conditional knock-in to cerebellar Purkinje cells (Pcp2Cre+/− Swap+/−) with mean age 203 ± 12 d, and 31 (18 male, 13 female) control mice (Pcp2Cre+/−) with mean age 200 ± 11 d. Four Pcp2-KI mutant (Pcp2Cre+/− Swap+/−) male mice were only included in motor behavior analysis: one was due to respiratory failure during neuroimaging, and three were due to data file corruption. All mice were maintained on a 12-h light/dark cycle with food and water *ad libitum*. All experiments were approved and monitored by the Institutional Animal

Care and Use Committee at the University of Florida and were conducted in ethical compliance with the USPHS Guide for Care and Use of Laboratory Animals.

2.3. Motor behavior tests and analysis

Locomotor function was evaluated for both the D2-KI cohort ($n = 59$, 30 control mice, 29 D2-KI mutant) and the Pcp2-KI cohort ($n = 68$, 31 control mice, 37 Pcp2-KI mutant) using the elevated beam-walking and accelerated rotarod (Ugo Basile) assessments, previously described by in Wilkes et al. (2021) and Yokoi et al. (2020). The beam-walking test assesses the coordination and balance of mice as they traverse beams of decreasing width and differing shapes. Mice were trained to traverse a medium square beam (14 mm width) across 3 trials each day for 2 consecutive days (6 total training trials). On day 3, mice performed 1 trial traversing a medium square (14 mm width) and 1 trial traversing a medium round beam (17 mm diameter). Day 4 included 1 testing trial traversing a small square (7 mm width) and 1 trial traversing a small round beam (10 mm diameter). All beams were 100 cm in length and total beam slips were recorded for the middle 80 cm section. The number of hind paw slips on each side was counted by investigators blind to the genotypes.

The accelerated rotarod test assesses the ability of mice to maintain balance and coordination on an accelerating rotating rod. The apparatus started at an initial speed of 4 rpm, and then the mouse was put on a slot before the rod speed was gradually accelerated at a rate of 0.2 rpm/s. The latency to fall was measured with a cutoff time of 3 min at a final rate of 40 rpm. Each mouse was placed in the same slot on the apparatus to minimize variation. Mice were tested on 2 days, with 3 trials per day. Between trials on the same day, mice were given a 1-h rest interval. Rotarod and beam-walking testing occurred within 15–30 days prior to imaging for all animals.

Data were then tested for normality using the SAS 9.4 statistical package. Both beam-walking and rotarod data were not normally distributed, and thus were analyzed using the non-parametric GENMOD procedure in SAS with a negative binomial distribution (Dang et al., 2005; Wilkes et al., 2021). Two-way interactions between genotype and age, weight, beam, side, trial, and sex were explored first, and if found to be significant, included in the final "reduced" model. Although clinically DYT1 dystonia has no sex predominance (Meoni et al., 2020), the basal ganglia and cerebellum have sexual dimorphism (Raz et al., 2001; Rijpkema et al., 2012). Because our models targeted these brain regions, we checked for any existing sex predominance by performing additional behavioral analysis separately for each sex in beam-walking and rotarod tasks. For beam-walking, our analysis only focused on aggregate performance on the small and medium beams on days 3 and 4 of testing, in order to account for learning effects that may have occurred during training on days 1 and 2. For rotarod analysis, mice remaining on the beam at 180 s were censored for survival analysis to determine a marginal hazard ratio. Effects were considered significant at $p < 0.05$.

2.4. MRI preparation and scan parameters

Animal preparation for MRI was performed as previously described in (Wilkes et al., 2021). Briefly, before scanning mice were induced under general anesthesia via isoflurane delivered through a Surgivet vaporizer (Dublin, OH) and then maintained at 1–1.5% isoflurane for the duration of imaging. Research suggests that sensory neurons in the dorsal horn of the spinal cord that respond to noxious stimuli have relatively spared firing rates under isoflurane anesthesia (Kim et al., 2007). The experimental setup for mouse imaging is depicted in Fig. 1. Respiration was monitored using a respiration pad (SA Instruments, Stony Brook, NY) placed beneath the abdomen. Core body temperature was maintained using an in-house recirculating waterbed heating system and monitored via a thermal rectal probe (SA Instruments, Stony Brook, NY). A 256 mm^2 MR compatible advanced thermal stimulator (ATS) thermode (PATHWAY System, Medoc Advanced Medical Systems, Ramat Yishay, Israel) was affixed to the right plantar hind paw, which delivered heat stimulation during imaging.

MRI data were acquired on an 11.1 Tesla Magnex Scientific 40 cm horizontal magnet (Agilent, Inc. Palo Alto, CA, USA) with RRI BFG-240/120-S6: bore size 120 mm, Gmax = 1000 mT/m @325A with 200 μs rise time. B^1 excitation and signal detection were achieved using an in-house 2.5 × 3.5 cm quadrature surface transmit/receive mouse head coil tuned to 470.7 MHz (^{1}H resonance) (AMRIS, University of Florida). Scan sequences were prepared and controlled using ParaVision, Version 6.0.1 (Bruker BioSpin, Billerica, MA). Four types of MRI scans were acquired for every animal: an anatomical scan, sensory-evoked fMRI, resting-state fMRI, and diffusion MRI.

Anatomical T2-weighted images were acquired for spatial normalization using a turbo RARE sequence with the following parameters: TR = 5500 ms; TE = 30 ms; excitation angle = 90°; refocusing angle = 180°; dummy scans = 1; averages = 7; slices = 13; orientation = coronal; thickness = 0.9 mm; gap = 0 mm; FOV = 15 × 15 mm; data matrix = 256 × 256 in-plane.

Sensory-evoked and resting-state fMRI scans were acquired using a 2-shot EPI sequence with the following parameters: TR = 2000 ms; TE = 15 ms; repetitions = 360 (sensory-evoked fMRI) or 180 (resting-state fMRI); flip angle = 90°; dummy scans = 2; slices = 13; coronal orientation; thickness = 0.9 mm; gap = 0 mm; FOV = 15 × 15 mm; data

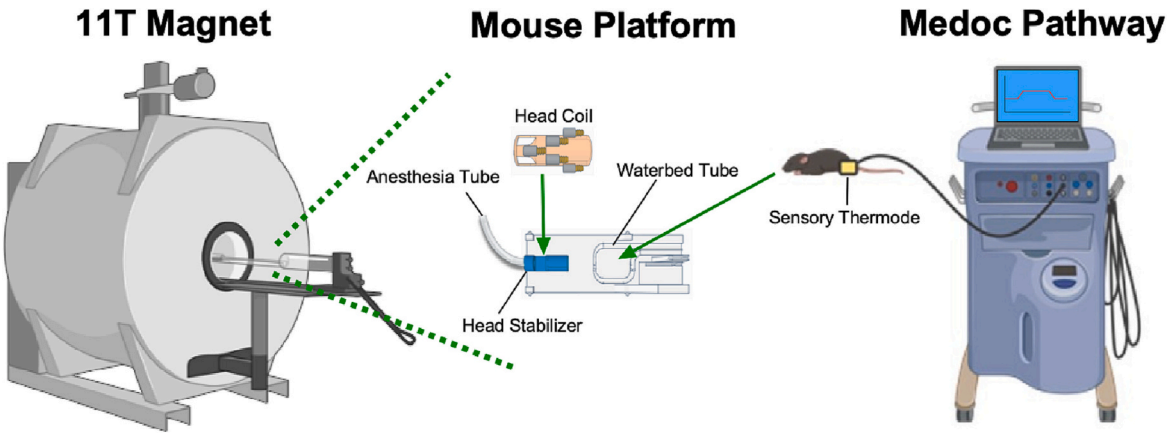

Fig. 1. Imaging setup. Imaging was performed on an 11.1 Tesla MRI scanner with a Magnex Scientific 40 cm horizontal magnet (Bruker BioSpin, Billerica, MA). For imaging, animals were placed on a custom-designed mouse platform, which included anesthesia provided through a head stabilizer with a surface transmit/receive radiofrequency head coil. Core body temperature was maintained during imaging with a heated waterbed tube placed underneath the animal. A Medoc PATHWAY heating thermode was placed on the right hindlimb of the animal and controlled by an associated computer setup.

acquisition matrix = 64 × 64 in-plane.

Diffusion MRI scans were acquired using an EPI sequence with the following parameters: TR = 4000 ms; TE = 19 ms; averages = 4; flip angle = 90°; slices = 17; orientation = coronal; thickness = 0.7 mm; gap = 0 mm; FOV = 15 × 11 mm; data matrix = 128 × 96 in-plane. The following diffusion parameters were used: one non-diffusion weighted b0 images; b-value = 2000 s/mm^2; directions = 46.

2.5. Sensory-evoked fMRI thermal stimulation

Acquisition of sensory-evoked fMRI involved heat-induced stimulation of the right plantar hind paw. The PATHWAY System was calibrated such that thermal stimulation was applied in a block paradigm alternating between 60 s at the stimulation temperature (42 °C) and 60 s at the baseline temperature (30 °C), beginning and ending with a 30 s baseline block. The change in temperature between blocks was achieved within 300 ms via a cooling rate of 40 °C/s and a heating rate of 70 °C/s.

2.6. fMRI preprocessing

Data processing for sensory-evoked and resting-state fMRI scans were performed similar to Chu et al. (2020), using custom-designed UNIX shell scripts with commands from Analysis of Functional NeuroImages (AFNI; Cox, 1996) and Advanced Normalization Tools (ANTs; Avants et al., 2010). The fMRI processing pipeline was automated and could, therefore, be applied equally and without bias to all scans. We acquired 2 duplicate scans from each type of fMRI paradigm (sensory-evoked and resting-state). For sensory-evoked fMRI, the 2 duplicate scans were processed identically and used as a repeated measure within subjects. For resting-state fMRI, we concatenated the data from the 2 duplicate scans, such that resting-state data were analyzed as a single time series. Data were only excluded from sensory-evoked and resting-state fMRI analysis due to excessive motion that prevented deconvolution of the hemodynamic response function.

The first 5 TRs were removed from each fMRI scan to account for signal equilibration. Outliers within each voxel's time series were identified using 3dToutcount in AFNI, and volumes with >5% of the total voxels determined to be outliers were flagged for exclusion during regression. Scan data were then despiked, slice-time corrected, corrected for motion and distortion via alignment to the first volume (3dvolreg, AFNI), spatially smoothed with a 0.3 mm full width half maximum (FWHM) Gaussian kernel, and scaled to have a range of (0,200) and mean of 100. For resting-state fMRI data, we also applied bandpass filtering of the time series between 0.01 and 0.1 Hz. The matrix derived from motion-correction was used to compute demeaned and derivatives of motion parameters for use as regressors. Volumes in which the Euclidian norm of the derivative values exceeded 0.5 were flagged for exclusion during regression. Brain masks were created on high-resolution anatomical scans and then registered to the fMRI scan from the same animal in order to remove signal from voxels outside the brain. In order to spatially normalize data, fMRI images from each mouse were registered to the T2-weighted anatomical scan from the same animal, and then to a high-resolution T2-weighted mouse template brain, generated from anatomical scans of 160 mice (Chu et al., 2020). We evaluated 12 regions of interest (ROIs) from key areas of the sensorimotor network, which were selected based on their relevance to the pathophysiology of dystonia (DeSimone et al., 2016, 2017; MacIver et al., 2022; Wilkes et al., 2021). Some regions that are pertinent to dystonia were not included for ROI analysis, due to their small size and lack of nearby landmarks for reliable segmentation (e.g., pedunculopontine nucleus). These ROIs are depicted on the mouse anatomical template brain in Fig. 2B.

2.7. Sensory-evoked fMRI analysis

We determined the sensory-evoked hemodynamic response time series using a response function convolved with 20 "tent" or piecewise linear B-spline basis functions which capture the percent change for the blood oxygenation level dependent (BOLD) signal across time (Saad et al., 2006), spanning 80 s from the onset of each stimulation block. Preprocessed data were regressed to these simulated tent response functions, with six motion parameters calculated during motion correction also accounted for by including them as regressors of no interest. Volumes flagged with excessive motion by 3dToutcount were censored in this step and excluded from the regression analysis. The β-coefficients of the regressed time series (one for each tent) and the corresponding t-statistics, were the dependent variables at this level of analysis. At this stage of the analysis, 2 control mice from the D2-KI cohort (1 male and 1 female) were excluded due to excessive motion that prevented deconvolution of the hemodynamic response function.

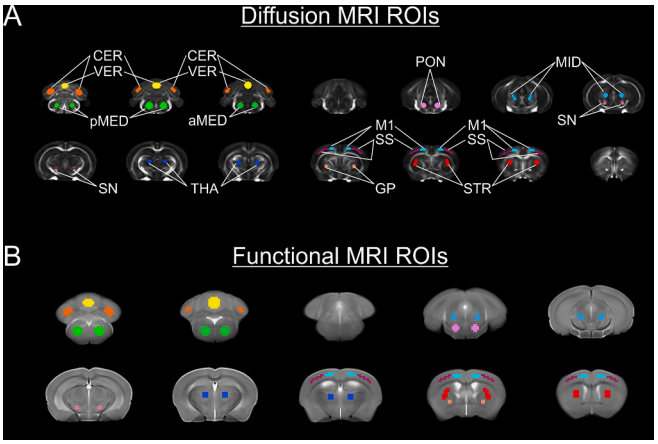

Fig. 2. Regions of Interest. The top panel (A) shows diffusion MRI regions of interest overlaid on top of the fractional anisotropy template image: cerebellum (CER; orange), vermis (VER; yellow), posterior medulla (pMED; light green), anterior medulla (aMED; dark green), pons (PON; pink), midbrain (MID; turquoise), substantia nigra (SN; magenta), thalamus (THA; dark blue), globus pallidus (GP; orange), somatosensory cortex (SS; purple), primary motor cortex (M1; light blue), and striatum (STR; red). (For interpretation of the references to colour in this figure legend, the reader is referred to the web version of this article.)

The sensory-evoked fMRI data were then transformed to the mouse T2 template (as described in section 2.6). We extracted values of the 20 β-coefficients representing the hemodynamic response time series from 0 to 80 s after hind paw thermal stimulation, from each of the 12 ROIs. Although hind paw stimulation was performed unilaterally, we evaluated the brain's response to the stimulus bilaterally because unilateral heat stimulation has been shown to result in bilateralBOLD response in mice (Bosshard et al., 2015; Chu et al., 2020).

For statistical analysis of sensory-evoked fMRI data, we performed repeated measures analysis of covariance for each ROI using SPSS Statistics 27 (IBM; Armonk, New York). Between-subjects factors were genotype and sex, duplicate scans (scan 1 and 2) and the sensory-evoked BOLD time series were considered as within-subjects factors, and age as a covariate. Our primary interest was the sustained portion of the sensory-evoked signal (20–60s after stimulus onset), and thus the BOLD time series included for statistical analysis were the corresponding 10 tent functions reflecting the signal change in the time period 20–60s after stimulus onset.

2.8. Resting-state fMRI analysis

Concatenated and preprocessed resting-state fMRI data were subjected to general linear regression. As with sensory-evoked fMRI scans, volumes flagged with excessive motion by 3dToutcount were censored and excluded from the regression analysis. At this stage of the resting-state fMRI analysis, 1 female control mouse from the D2-KI cohort was

excluded due to excessive motion. We then applied additional regressors for the mean signal from cerebrospinal fluid (CSF) and the first-order derivatives of the motion parameters calculated during motion correction as this has been suggested to improve resting-state functional connectivity analysis (Satterthwaite et al., 2013). We then performed seed-to-voxel resting-state functional connectivity analysis. We extracted the mean signal of all voxels within a particular ROI for each time point in the concatenated time series, which was then correlated with the time series of each voxel throughout the brain to generate a whole brain map of functional connectivity. This was done for each of the 12 ROIs.

For resting-state fMRI data, we analyzed functional connectivity using seed-to-voxel approach. We did not observe significant effects of sex on resting-state functional connectivity and thus applied voxelwise *t*-tests to identify between-group effects for each cohort. For each of the 12 ROIs, between-group statistics (mutant *vs.* control) were performed at every voxel in the brain using AFNI. In order to control for false-positives across voxels, a one-sample t-test was performed using AFNI's *Clustsim* bootstrapping option to advise the cluster-extent threshold. *Clustsim* advises a minimum number of significant (uncorrected) voxels for a cluster to be considered significant while controlling for false-positives at our desired alpha of 0.05 (Cox et al., 2017) and is functionally similar to other approaches for controlling for multiple comparisons. *Clustsim* calculations were performed separately for the D2-KI and Pcp2-KI cohorts using the voxel-level threshold of $p < 0.01$ and nearest neighbor (NN3) clusterization. In accordance with the advised cluster threshold, between-group effects were considered significant ($p_{corrected} < 0.05$) at a minimum cluster size of 12 voxels (0.59 mm^3) for the D2-KI cohort, and also coincidentally a minimum cluster size of 12 voxels (0.59 mm^3) in the Pcp2-KI cohort.

2.9. Diffusion MRI processing and analysis

Data processing for diffusion MRI was performed similar to Chu et al. (2020), using custom-designed UNIX shell scripts with commands from AFNI (Cox, 1996), FMRIB Software Library (FSL; Jenkinson et al., 2012) and ANTs (Avants et al., 2010). The diffusion MRI processing pipeline was automated and could, therefore, be applied equally and without bias to all scans. Data were corrected for motion and eddy currents using affine transform with FSL's eddy correct function. Diffusion MRI data for three control mice from the D2-KI cohort and two mutant mice from the Pcp2-KI cohort were discarded due to high motion-related distortions. The resultant transformation matrix was used to rotate diffusion-weighted directions (i.e., b-vectors) accordingly, in order to properly estimate the diffusion tensor and diffusion parameters after eddy correction. Estimation of diffusion parameters was calculated using a two-compartment model to account for partial volume effects of extracellular free-water. We utilized publicly available workflow for single shell free water elimination and estimation of diffusion parameters (https://github.com/sameerd/DiffusionTensorImaging), implemented through MATLAB and the DIPY imaging library in Python 3.6 (Garyfallidis et al., 2014). The resultant maps of free-water (FW) and free-water corrected FA (FA_T) were variables of interest for this analysis.

In order to spatially normalize data, FA_T images from each mouse were nonlinearly registered to a FA_T mouse template brain, generated from FA_T maps of 160 mice (Chu et al., 2020). Because diffusion scans had a high in-plane resolution (117 × 115 μm) with a relatively large slice thickness (700 μm), we performed nonlinear registration to the template in a slice-by-slice fashion in order to prevent possible warping between slices. The transformation matrices derived from registration of the FA_T scans to the template were then applied to the FW image from the same animal.

For statistical analysis of diffusion MRI data, we performed multivariate analyses of covariance using SPSS Statistics 27 (IBM; Armonk, New York). Between-subjects factors were genotype and sex, with age as a covariate. We analyzed between-group differences in FW and FA_T for the same 12 ROIs that were utilized in fMRI analyses, transformed into diffusion MRI space (Fig. 2A). Group effects were considered significant at $p < 0.05$.

3. Results

3.1. D2-KI motor deficits and Pcp2-KI motor improvements

For the D2-KI cohort there was a significant genotype effect, such that mutant mice had increased average beam-walking slips ($p = 0.039$) compared to controls (Fig. 3A; Table 1). There were no significant interactions of genotype with age, weight, beam type, side, trial, batch, or sex (Supplementary Table 1A), and as such these factors were not included in the reduced model (Table 1). For D2-KI rotarod testing, there was no significant effect of genotype on latency to fall (Table 1). For D2-KI rotarod testing, there were no significant interactions of genotype with age, weight, sex, and trial (Supplementary Table 1B). Separate analysis for male and female D2-KI mice showed that neither sex had significant genotype effect in beam-walk or rotarod performance (Table 1).

For the Pcp2-KI cohort, there was no significant effect of genotype on average beam-walking slips (Table 1). There were no significant interactions of genotype with age, weight, beam type, side, trial, batch, or sex on beam-walking slips (Supplementary Table 1A). For Pcp2-KI rotarod testing, there was a significant effect of genotype in the full model ($p = 0.043$), but there were no significant interactions of genotype with age, weight, sex, and trial (Supplementary Table 1B). The full

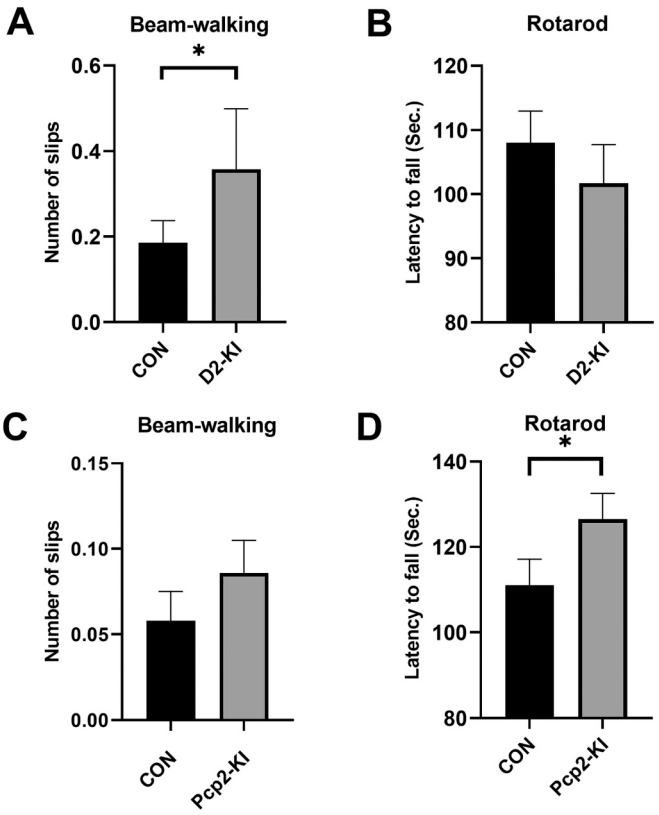

Fig. 3. Motor performance in D2-KI and Pcp2-KI mice. In the D2-KI cohort, mutant mice displayed a significant (*$p < 0.05$, reduced model) beam-walking deficit (A), but no difference in rotarod performance (B). In contrast, Pcp2-KI mutant mice showed no difference in beam-walking performance (C), but significantly improved performance (*$p < 0.05$ in the full model, $p = 0.069$ in the reduced model) on the rotarod (D). Data are shown as the mean number of slips for beam-walking and the mean latency to fall for rotarod (error bars: SEM).

Table 1
Mean ± SEM values are reported for beam-walking and rotarod tests in both the mutant and control mice from the D2-KI and Pcp2-KI cohorts. For both the genotypes, *p* values for genotype differences are reported for all the animals, for male-only and female-only analyses for the final "reduced" model.

		Mutant KI Mean ± SEM	Control Mean ± SEM	Genotype p value	Male only genotype p value Pval	Female only Genotype p value Pval
D2-KI	Beam-walking	0.358 ± 0.141	0.186 ± 0.052	0.039*	0.153	0.077
	Rotarod	101.73 ± 6.012	108.02 ± 4.956	0.356	0.637	0.100
Pcp2-KI	Beam-walking	0.086 ± 0.019	0.058 ± 0.017	0.245	0.063	0.809
	Rotarod	126.55 ± 5.980	111.01 ± 6.091	0.069	0.558	0.023*

model was reduced to a model with no two-way interactions of genotype with other variables. The removal of these other factors resulted in only a trend-level effect of genotype in the reduced model ($p = 0.069$). However, separate analysis for each sex (see Table 1) showed that female Pcp2-KI mutant mice had improved performance with greater latency to fall ($p = 0.023$) compared to controls, but male Pcp2-KI mutants and control mice showed no difference in latency to fall ($p = 0.558$).

3.2. Region specific differences in sensory-evoked activation in D2-KI and Pcp2-KI mice

For the D2-KI cohort, we observed a significant genotype by time series interaction ($p = 0.005$, $\eta^2 = 0.049$) in the somatosensory cortex (Fig. 4A), where initially the BOLD activation time series was similar between groups, but D2-KI mutant mice had a diminished response in the later sustained portion of the time series (Fig. 4B). There were no other significant effects observed in the somatosensory cortex for D2-KI cohort. There were no significant group effects or interactions in other ROIs (data not shown).

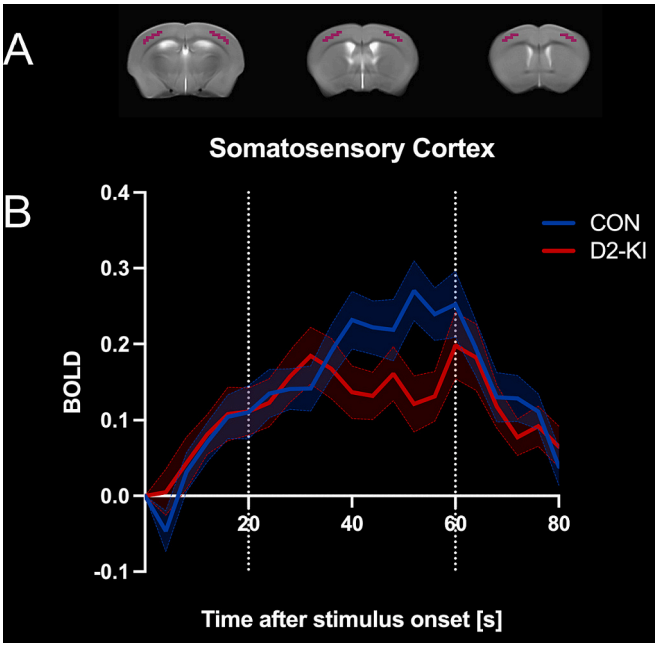

Fig. 4. D2-KI sensory-evoked BOLD. (A) The somatosensory cortex region of interest overlaid on top of mouse anatomical template image. (B) Blood oxygen level dependent (BOLD) percent signal change in the somatosensory cortex as a result of the sensory-evoked fMRI paradigm. There was a significant interaction between genotype and time-course, such that D2-KI mice (red) had blunted BOLD signal during the latter portion of sustained stimulus compared to controls (blue). (For interpretation of the references to colour in this figure legend, the reader is referred to the web version of this article.)

For the Pcp2-KI cohort we observed a significant effect of genotype in the striatum ($p = 0.038$, $\eta^2 = 0.070$; Fig. 5A-B) and midbrain ($p = 0.007$, $\eta^2 = 0.115$; Fig. 5C-D), with both ROIs showing lower BOLD activation in Pcp2-KI mutants compared to controls. There were no other significant main effects or interactions observed in the striatum or midbrain ROIs for the Pcp2-KI cohort. There were no significant group effects or interactions for sensory-evoked fMRI in the other 10 ROIs between Pcp2-KI mutant and control mice (data not shown).

3.3. Region specific differences in resting-state functional connectivity in D2-KI and Pcp2-KI mice

For the D2-KI cohort we observed a significant effect of genotype on functional connectivity of the anterior medulla, such that D2-KI mutant mice showed greater functional connectivity between the anterior medulla and a 14-voxel cluster localized in the secondary somatosensory cortex ($p_{corrected} < 0.05$; Fig. 6). We did not observe significant differences in resting-state functional connectivity for the other 11 ROIs between D2-KI mutant and control mice (data not shown).

For the Pcp2-KI cohort we observed a significant effect of genotype on functional connectivity of the striatum, such that Pcp2-KI mutant mice showed greater functional connectivity between the striatum and a 12-voxel cluster localized in the anterior medulla of the brainstem ($p_{corrected} < 0.05$; Fig. 7). We did not observe significant differences in resting-state functional connectivity for the other 11 ROIs between Pcp2-KI mutant and control mice (data not shown).

3.4. No genotype differences in diffusion MRI

For the D2-KI cohort we observed no significant effect of genotype or sex on FW in any of the 12 ROIs. There was no significant effect of genotype on FA_T for any of the 12 ROIs. We observed a significant effect of sex on FA_T in the cerebellum ($p = 0.013$) and substantia nigra ($p = 0.001$), neither of which had a significant genotype by sex interaction. Diffusion MRI statistics for the D2-KI cohort are summarized in Table 2A.

For the Pcp2-KI cohort we observed no significant effect of genotype or sex on FW in any of the 12 ROIs. There was no significant effect of genotype on FA_T for any of the 12 ROIs. We observed a significant effect of sex on FA_T in the cerebellum ($p = 0.001$), posterior medulla ($p < 0.001$), anterior medulla ($p < 0.001$), pons ($p = 0.014$), midbrain ($p = 0.007$), somatosensory cortex ($p = 0.043$) and substantia nigra ($p < 0.001$), none of which had a significant genotype by sex interaction. Diffusion MRI statistics for the D2-KI cohort are summarized in Table 2B. Although we observed no significant genotype by sex interactions in the Pcp2-KI cohort, we report those interaction *p*-values for the Pcp2-KI cohort in Table 1B because motor behavior in that cohort had a genotype by sex interaction.

4. Discussion

The basal ganglia and cerebellum are consistently linked to the pathophysiology of DYT1 dystonia, yet little is known about how specific torsinA dysfunction in these components contribute to abnormal network properties in the deeply interconnected sensorimotor network. In the present study, we used transgenic animal models to determine whether torsinA dysfunction caused by the *Dyt1* ΔGAG mutation in specific cells of the basal ganglia or cerebellum would generate sensorimotor dysfunction and brain changes associated with dystonia. We evaluated motor performance with beam-walking and rotarod tasks, sensory-evoked and resting-state fMRI to assess functional activation and connectivity, and dMRI to assess microstructure. The sensory-

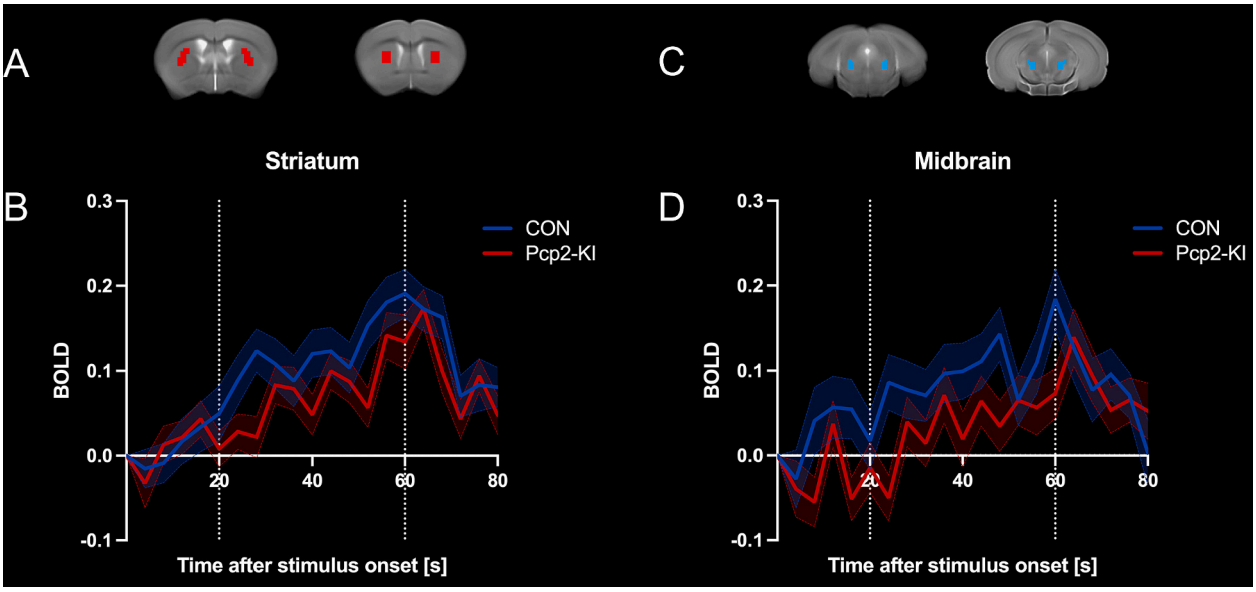

Fig. 5. Pcp2-KI sensory-evoked BOLD. The top panel shows regions of interest for the striatum (A) and midbrain (B) regions of interest overlaid on top of the mouse anatomical template image. The bottom panel shows sensory-evoked blood oxygen level dependent (BOLD) percent signal change in the striatum (C) and midbrain (D), which showed a significant effect of genotype such that Pcp2-KI mice (red) had lower BOLD signal during 20–60 period after stimulus onset compared to controls (blue) in both brain regions. (For interpretation of the references to colour in this figure legend, the reader is referred to the web version of this article.)

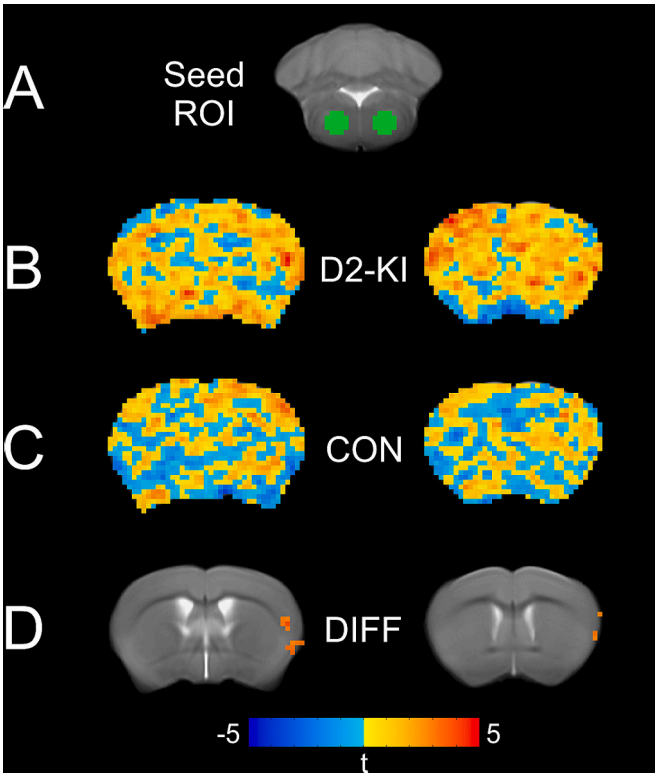

Fig. 6. D2-KI resting-state functional connectivity. Coronal slices representing functional connectivity from the anterior medulla seed (A). Group means are shown for D2-KI mutant mice (B) and control mice (C). Red colors show voxels with a high degree of functional connectivity and blue colors show voxels with low degree of functional connectivity. We observed significant differences ($p_{corrected} < 0.05$) in functional connectivity between D2-KI mutant and control mice, such that mutants had increased functional connectivity between the anterior medulla and a voxel cluster in the secondary somatosensory cortex (D). (For interpretation of the references to colour in this figure legend, the reader is referred to the web version of this article.)

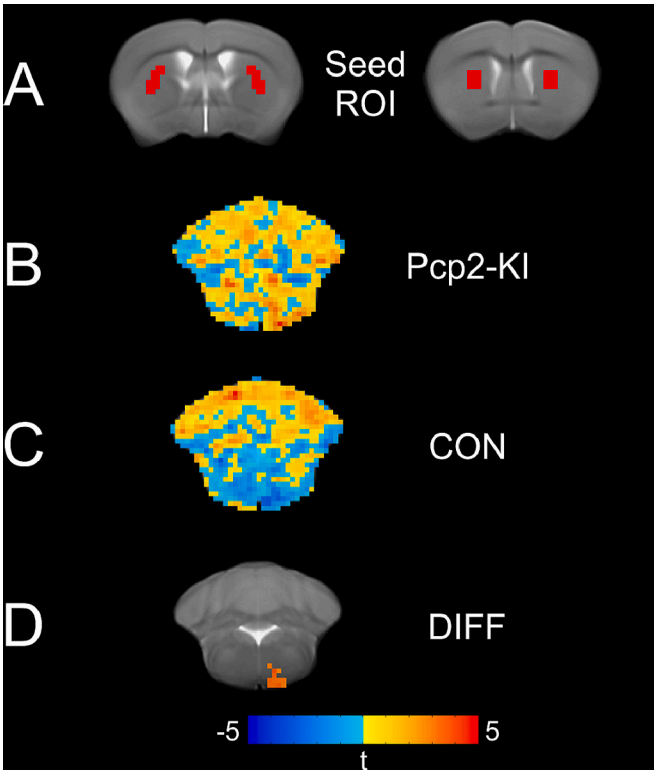

Fig. 7. Pcp2-KI resting-state functional connectivity. Coronal slices representing functional connectivity from the striatum seed (A). Group means are shown for Pcp2-KI mutant mice (B) and control mice (C). Red colors show voxels with a high degree of functional connectivity and blue colors show voxels with low degree of functional connectivity. We observed significant differences ($p_{corrected} < 0.05$) in functional connectivity between Pcp2-KI mutant and control mice, such that mutants had increased functional connectivity between the striatum and a voxel cluster in the medulla (D). (For interpretation of the references to colour in this figure legend, the reader is referred to the web version of this article.)

Table 2
Region of interest analysis for diffusion MRI measures of FW and FA_T in D2-KI (A) and Pcp2-KI (B) cohorts. Left column contains results for free water (FW) and right column contains results for free water corrected fractional anisotropy (FA_T). Mean ± standard deviation, and *p*-value are reported. *Abbreviations*: *anterior medulla (aMedulla); posterior medulla (pMedulla), globus pallidus (GP), primary motor cortex (M1), sensorimotor cortex (SS), and substantia nigra (SNr).*

(2A) D2-KI Study

Region of interest (ROI)	Free water (FW)				Free water corrected fractional anisotropy (FA_T)			
	D2-KI Mutant (*D2Cre*+/− *Swap*+/−) Mean ± stdev	D2-KI Control (*D2Cre*+/−) Mean ± stdev	Genotype p value	Sex p value	D2-KI Mutant (*D2Cre*+/− *Swap*+/−) Mean ± stdev	D2-KI Control (*D2Cre*+/−) Mean ± stdev	Genotype p value	Sex p value
Cerebellum	0.283 ± 0.029	0.282 ± 0.029	0.683	0.872	0.183 ± 0.026	0.185 ± 0.028	0.904	*0.013
Vermis	0.271 ± 0.029	0.272 ± 0.028	0.950	0.598	0.195 ± 0.034	0.200 ± 0.030	0.882	0.176
pMedulla	0.306 ± 0.026	0.309 ± 0.034	0.654	0.676	0.211 ± 0.036	0.220 ± 0.040	0.742	0.006
aMedulla	0.289 ± 0.026	0.289 ± 0.027	0.923	0.461	0.210 ± 0.028	0.220 ± 0.032	0.222	0.363
Pons	0.292 ± 0.023	0.285 ± 0.022	0.101	0.930	0.233 ± 0.030	0.228 ± 0.024	0.353	0.958
Midbrain	0.302 ± 0.020	0.308 ± 0.029	0.959	0.703	0.335 ± 0.027	0.335 ± 0.024	0.808	0.078
Thalamus	0.296 ± 0.015	0.292 ± 0.021	0.294	0.298	0.235 ± 0.045	0.230 ± 0.039	0.918	0.421
GP	0.282 ± 0.029	0.281 ± 0.028	0.731	0.945	0.312 ± 0.058	0.325 ± 0.061	0.567	0.835
Striatum	0.270 ± 0.016	0.269 ± 0.024	0.469	0.324	0.189 ± 0.022	0.188 ± 0.025	0.877	0.116
M1	0.273 ± 0.018	0.274 ± 0.025	0.652	0.612	0.178 ± 0.020	0.185 ± 0.024	0.242	0.940
SS	0.272 ± 0.020	0.271 ± 0.026	0.453	0.812	0.136 ± 0.018	0.138 ± 0.018	0.828	0.139
SNr	0.320 ± 0.013	0.318 ± 0.023	0.418	0.846	0.343 ± 0.029	0.333 ± 0.023	0.068	***0.001

(2B) Pcp2-KI study

Region of interest (ROI)	Free water (FW)					Free water corrected fractional anisotropy (FA_T)				
	Pcp2-KI Mutant (*Pcp2Cre*+/− *Swap*+/−) Mean ± stdev	Pcp2-KI Control (*Pcp2Cre*+/−) Mean ± stdev	Genotype p value	Sex p value	Genotype * Sex p value	Pcp2-KI Mutant (*Pcp2Cre*+/− *Swap*+/−) Mean ± stdev	Pcp2-KI Control (*Pcp2Cre*+/−) Mean ± stdev	Genotype p value	Sex p value	Genotype * Sex p value
Cerebellum	0.297 ± 0.035	0.303 ± 0.037	0.374	0.766	0.327	0.197 ± 0.029	0.209 ± 0.038	0.139	**0.001	0.556
Vermis	0.283 ± 0.038	0.281 ± 0.038	0.886	0.922	0.183	0.217 ± 0.036	0.225 ± 0.039	0.367	0.372	0.124
pMedulla	0.315 ± 0.028	0.322 ± 0.033	0.379	0.600	0.218	0.219 ± 0.029	0.225 ± 0.036	0.580	***0.000	0.650
aMedulla	0.305 ± 0.042	0.311 ± 0.083	0.518	0.139	0.166	0.239 ± 0.045	0.245 ± 0.052	0.511	***0.000	0.840
Pons	0.305 ± 0.033	0.301 ± 0.035	0.778	0.332	0.269	0.247 ± 0.035	0.249 ± 0.038	0.852	*0.014	0.959
Midbrain	0.319 ± 0.027	0.313 ± 0.025	0.459	0.926	0.355	0.348 ± 0.029	0.339 ± 0.028	0.239	**0.007	0.474
Thalamus	0.308 ± 0.028	0.308 ± 0.027	0.978	0.778	0.573	0.204 ± 0.035	0.206 ± 0.039	0.940	0.536	0.190
GP	0.306 ± 0.028	0.304 ± 0.024	0.922	0.703	0.270	0.369 ± 0.067	0.346 ± 0.062	0.357	0.951	0.346
Striatum	0.291 ± 0.029	0.289 ± 0.024	0.868	0.777	0.984	0.189 ± 0.028	0.190 ± 0.028	0.663	0.539	0.999
M1	0.297 ± 0.027	0.297 ± 0.022	0.953	0.768	0.637	0.187 ± 0.025	0.198 ± 0.026	0.104	0.105	0.968
SS	0.296 ± 0.029	0.294 ± 0.024	0.908	0.771	0.666	0.153 ± 0.026	0.156 ± 0.026	0.600	*0.043	0.888
SNr	0.333 ± 0.018	0.329 ± 0.0019	0.502	0.490	0.525	0.347 ± 0.029	0.339 ± 0.026	0.235	***0.000	0.775

evoked fMRI paradigm in this study was implemented based on the framework that the somatosensory system has a major role in the pathophysiology of dystonia (Tinazzi et al., 2003), and that sensory load may reveal functional deficits to the system that are not observed at rest. We found that D2-KI mutant mice had motor deficits, abnormal sensory-evoked brain activation in the somatosensory cortex, as well as increased functional connectivity of the anterior medulla with cortex. In contrast, we found that Pcp2-KI mice had improved motor performance, reduced sensory-evoked brain activation in the striatum and midbrain, as well as reduced functional connectivity of the striatum with the anterior medulla. We included age as a covariate in behavioral and MRI analyses, and thus our statistics do not suggest that age had a significant impact on the observed results. These findings suggest that (1) D2 cell-specific *Dyt1* ΔGAG mediated torsinA dysfunction in the basal ganglia results in detrimental effects on the sensorimotor network and motor output, and (2) Purkinje cell-specific *Dyt1* ΔGAG mediated torsinA dysfunction in the cerebellum results in changes to the sensorimotor network that may be compensatory and protect against dystonia-like motor deficits.

The reduced sensory-evoked activation observed in both D2-KI and Pcp2-KI mutant mice occurred in different components of the sensorimotor network and had divergent effects on motor performance. In D2-KI mutant mice the activation deficit in the somatosensory cortex was time-dependent, such that there was no difference in the first 20s of

stimulation, but signal was blunted in the latter portion of the time series (Fig. 4). Our prior work in cell-specific D2KO mice similarly showed motor deficits and blunted sensory-evoked activation in a portion of sensorimotor cortex, but was not time-dependent (Wilkes et al., 2021). Interestingly, sensory abnormalities reported in human dystonia include impaired temporal processing of sensory stimuli in dystonia patients and some non-manifesting DYT1 mutation carriers (Bradley et al., 2012; Fiorio et al., 2007; Conte et al., 2017). Our observation in D2-KI mice more closely matches this aspect of sensorimotor abnormalities seen in human dystonia than was previously observed in D2KO mice, possibly because the KI model recapitulates the ΔGAG mutation found in early-onset primary dystonia.

The sensory-evoked activation pattern differed in Pcp2-KI mutant mice, where we found reduced activity in the striatum and midbrain over the entire 20–60s after stimulus onset. Although the cerebellum processes both sensory and motor information, these networks have complex representation and a great degree of integration at the level of the cerebellar cortex, where single regions of the cerebellar cortex may project to broad targets in the forebrain (Pisano et al., 2021). In addition, it has been demonstrated that the sensory-associated cerebellar vermis receives input from cortical motor regions in the forebrain (Coffman et al., 2011). It is possible that *Dyt1* ΔGAG-mediated torsinA dysfunction in Purkinje cells has complex effects on motor output and sensory processing, given that the Pcp2-KI was not designed to target specific sub-populations of Purkinje neurons. This study cannot conclusively determine whether the reduced sensory-evoked activity we observed in the striatum and midbrain of Pcp2-KI mutant mice represents a true sensory processing deficit or rather compensatory changes to the system. Given that there was no significant motor deficit in Pcp2-KI mutant mice as a whole, which entails a great degree of sensorimotor integration, we do not believe our neuroimaging findings to represent a sensory processing deficit in Pcp2-KI mutant mice. It is interesting that while male Pcp2-KI mice showed no motor deficit compared to male controls, female Pcp2-KI mutant mice showed improved rotarod performance over female controls, possibly representing an interaction of the *Dyt1* ΔGAG mutation with estrogen in modulating glutamatergic signaling in the cerebellum (Hedges et al., 2012). One interpretation of our neuroimaging findings is that sensory domain cortico-striatal projections have reduced gain. Indeed, long-term depression (LTD) of corticostriatal projections was found in mice with whole-brain *Dyt1* ΔGAG KI (Dang et al., 2012) and LTD has been associated with reduced BOLD activity in fMRI (Rottmann et al., 2010). Although we observed no sex differences on functional neuroimaging measures, there is evidence from human neuroimaging studies of sex differences in the cerebellum, particularly the vermis (Raz et al., 2001).

Analyses of resting-state functional connectivity provided information about the sensorimotor network without a sensory load. In D2-KI mutant mice there was greater functional connectivity between the anterior medulla and a portion of the secondary somatosensory cortex. In Pcp2-KI mutant mice there was greater functional connectivity between the striatum and anterior medulla. Prior work in whole-brain *Dyt1* ΔGAG KI similarly showed altered functional connectivity of the striatum (DeSimone et al., 2016), which has also been observed in patients with DYT1 dystonia (Mazere et al., 2021). Moreover, resting-state functional connectivity deficits in the sensorimotor network were observed in clinically manifesting DYT1 mutation carriers, but were absent in non-manifesting mutation carriers (Premi et al., 2016). It is important to note that basal ganglia and cerebellar networks were not compared by Premi et al. (2016), as methodological limitations prevented construction of common subcortical networks across patients.

Structural alterations to the basal ganglia, cerebellum, and other components of the sensorimotor network have been reported in human dystonia (see MacIver et al., 2022). Microstructural differences have also been reported in the basal ganglia and cerebellum in *Dyt1* ΔGAG KI mice (DeSimone et al., 2016; Song et al., 2014; Song et al., 2013; Uluğ et al., 2011). The D2-KI and Pcp2-KI models utilized in this study are cell-specific versions of the *Dyt1* ΔGAG KI mouse model. However, this study did not find microstructural changes in either D2-KI or Pcp2-KI mutant mice. Previous work has reported lower FA in the striatum of *Dyt1* KI mice (Uluğ et al., 2011), and *Dyt1* KO mice had lower FA in the sensorimotor cortex and brainstem (Vo et al., 2015a). It is important to note that both of those investigations were performed using ex vivo methods for dMRI, which permits long scan times and higher spatial resolution than is possible in vivo. It may be that we did not detect microstructural changes in D2-KI and Pcp2-KI models because they occur on a smaller scale than our paradigm was sensitive to. For in vivo dMRI in this study slice thickness was set to 0.7 mm (700 μm) in order to achieve feasible scan times and acceptable signal-to-noise ratio, compared to the 0.0625 mm (62.5 μm) isotropic voxel size used for ex vivo dMRI by Uluğ et al. (2011) and Vo et al. (2015a). Most methodologically similar to the present study, DeSimone et al. (2016) performed in vivo dMRI in *Dyt1* KI mice and reported increased free-water in the striatum and cerebellum. All three of these papers that reported microstructural differences were performed in the *Dyt1* KI model, where the whole brain was affected by torsinA mutation. It may be that microstructure is more impacted when torsinA dysfunction occurs throughout the brain, rather than in specific neuronal populations.

In the D2-KI model, targeted cell types were medium spiny neurons of the indirect pathway, striatal cholinergic interneurons, and dopaminergic neurons of the basal ganglia. D2-KI mutant mice showed motor performance deficits and impaired sensory-evoked activation in the somatosensory cortex. These observations could represent impaired thalamocortical output from the basal ganglia. Supporting this notion, neuroimaging in human dystonia revealed impaired thalamocortical connectivity that was mediated by phenotypic variability, whereas corticostriatal and corticospinal pathways were not different between groups (Vo et al., 2015b). Our D2-KI resting-state functional connectivity findings also fit in this framework: deficient thalamocortical output from the basal ganglia could result in a compensatory change where signals between the cortex and medulla are amplified to overcome for the low gain of thalamocortical relays.

In contrast, there were no motor deficits in Pcp2-KI mutants, and we observed improved motor performance in female Pcp2-KI mutants. This finding is novel but matches our hypothesis based on prior work in the Purkinje cell-specific *Dyt1* KO model (Yokoi et al., 2012; Zhang et al., 2011). In the Pcp2-KI model, *Dyt1* ΔGAG mutation is restricted to cerebellar Purkinje cells, and the cerebellum (particularly Purkinje cells) shows a greater degree of sexual dimorphism than many other areas of the brain (Abel et al., 2011; Raz et al., 2001); this may partially explain the improved performance in female Pcp2-KI mutants, but no differences in males. We also observed reduced sensory-evoked activation in the striatum and midbrain of Pcp2-KI mutant mice, along with increased functional connectivity between the striatum and medulla. It is possible that the observed effects on motor behavior are mediated by reduced Purkinje cell output to the dentate nucleus. In support of this interpretation, electrophysiological recordings from the cerebellum of *Dyt1* KI mice showed non-tonically firing Purkinje cells had lower peak frequency, more pauses between bursting activity, and higher coefficient of variation compared to control mice (Liu et al., 2020). Another study that knocked down torsinA expression in adult wild-type mice also reported decreased firing rate of cerebellar Purkinje cells, but their manipulation induced dystonic symptoms (Fremont et al., 2017). These different outcomes in relation to a similar reduction of Purkinje cell firing may be explained by the presence of ΔGAG mutant torsinA throughout development, as the same manipulation in juvenile animals failed to induce dystonic symptoms, or by unintended effects of the shRNA knockdown approach in adult animals that do not naturally occur in DYT1 genetic dystonia. In human DYT1 dystonia, structural neuroimaging differences in the cerebellothalamic tract were reported to distinguish non-manifesting and clinically manifesting DYT1 mutation carriers — both groups showed alterations in a portion of the cerebellothalamic tract proximal to the cerebellum, but nonmanifesting carriers showed an

additional compensatory alteration in a distal portion of the cerebellothalamic tract (Argyelan et al., 2009). In cervical dystonia, repetitive transcranial magnetic stimulation (rTMS) to the cerebellum, using a stimulation paradigm designed to reduce firing of underlying neuronal populations, was found to improve motor symptoms (Koch et al., 2014). Although we observed differences in areas other than the cerebellum itself, the cited studies provide a possible mechanism to interpret the finding of improved motor behavior in Pcp2-KI mice: modified cerebellar output might exert protective effects on sensorimotor circuitry against dystonic motor symptoms. It remains unclear whether the observed effects on motor behavior and sensory-evoked fMRI in Pcp2-KI mice were mediated by shared or distinct mechanisms.

Investigating cell-specific torsinA dysfunction is crucial for understanding the complex network of pathophysiology in DYT1 dystonia. Considered together, our findings in the D2-KI and Pcp2-KI strains can help to elucidate components of the sensorimotor circuit which may be sensitive to effects of ΔGAG mutant torsinA. Prior evidence does not suggest there is impairment of the ascending sensory pathway from the spinal cord to somatosensory cortex in dystonia (Conte et al., 2019). In the present study, it is interesting that atypical activation and connectivity patterns in both mouse models did not occur in the targeted brain area, but rather in downstream components of the sensorimotor network — lending further support to the conceptualization of dystonia as a network disorder (Simonyan, 2018). The importance of the cerebellum in dystonia has become more widely appreciated, and recent focus has shifted to possible therapeutic effects achieved by targeting the cerebellum or its outputs to the thalamus (Chen et al., 2014; Tewari et al., 2017). This study's findings make an impactful contribution toward our understanding of neurological mechanisms mediating motor outcomes in DYT1 dystonia and may inform future research toward a cure.

Declaration of Competing Interest

The authors report no conflict of interest or competing financial interests to disclose.

Data availability

Data will be made available on request.

Acknowledgements

This work was supported by the National Institutes of Health (Project Number R01NS075012), and the Department of Defense (W81XWH1810099 and W81XWH2110198). F Yokoi and Y Li were partially supported by the Office of the Assistant Secretary of Defense for Health Affairs through the Peer-Reviewed Medical Research Program Discovery Award. Opinions, interpretations, conclusions, and recommendations are those of the author and are not necessarily endorsed by the Department of Defense. A portion of this work was performed in the McKnight Brain Institute at the National High Magnetic Field Laboratory's Advanced Magnetic Resonance Imaging and Spectroscopy (AMRIS) Facility, which is supported by National Science Foundation Cooperative Agreement No. DMR-1644779 and the State of Florida. This work was also supported in part by an NIH award, S10RR025671, for MRI/S instrumentation.

Appendix A. Supplementary data

Supplementary data to this article can be found online at https://doi.org/10.1016/j.expneurol.2023.114471.

References

Abel, J.M., Witt, D.M., Rissman, E.F., 2011. Sex differences in the cerebellum and frontal cortex: roles of estrogen receptor alpha and sex chromosome genes. Neuroendocrinology 93, 230–240. https://doi.org/10.1159/000324402.

Albanese, A., Bhatia, K., Bressman, S.B., DeLong, M.R., Fahn, S., Fung, V.S.C., Hallett, M., Jankovic, J., Jinnah, H.A., Klein, C., Lang, A.E., Mink, J.W., Teller, J.K., 2013. Phenomenology and classification of dystonia: a consensus update: dystonia: phenomenology and classification. Mov. Disord. 28, 863–873. https://doi.org/10.1002/mds.25475.

Argyelan, Miklos, Carbon, M., Niethammer, M., Ulug, A.M., Voss, H.U., Bressman, S.B., Dhawan, V., Eidelberg, D., 2009. Cerebellothalamocortical connectivity regulates penetrance in dystonia. J. Neurosci. 29, 9740–9747. https://doi.org/10.1523/JNEUROSCI.2300-09.2009.

Avants, B.B., Yushkevich, P., Pluta, J., Minkoff, D., Korczykowski, M., Detre, J., Gee, J.C., 2010. The optimal template effect in hippocampus studies of diseased populations. Neuroimage 49, 2457–2466. https://doi.org/10.1016/j.neuroimage.2009.09.062.

Bosshard, S.C., Stuker, F., von Deuster, C., Schroeter, A., Rudin, M., 2015. BOLD fMRI of C-Fiber mediated nociceptive processing in mouse brain in response to thermal stimulation of the forepaws. PLoS One 10, e0126513. https://doi.org/10.1371/journal.pone.0126513.

Bradley, D., Whelan, R., Kimmich, O., O'Riordan, S., Mulrooney, N., Brady, P., Walsh, R., Reilly, R.B., Hutchinson, S., Molloy, F., Hutchinson, M., 2012. Temporal discrimination thresholds in adult-onset primary torsion dystonia: an analysis by task type and by dystonia phenotype. J. Neurol. 259, 77–82. https://doi.org/10.1007/s00415-011-6125-7.

Burciu, R.G., Hess, C.W., Coombes, S.A., Ofori, E., Shukla, P., Chung, J.W., McFarland, N. R., Wagle Shukla, A., Okun, M.S., Vaillancourt, D.E., 2017. Functional activity of the sensorimotor cortex and cerebellum relates to cervical dystonia symptoms. Hum. Brain Mapp. 38, 4563–4573. https://doi.org/10.1002/hbm.23684.

Burke, R.E., Fahn, S., Marsden, C.D., 1986. Torsion dystonia: a double-blind, prospective trial of high-dosage trihexyphenidyl. Neurology 36, 160–164. https://doi.org/10.1212/wnl.36.2.160.

Carbon, M., Kingsley, P.B., Tang, C., Bressman, S., Eidelberg, D., 2008. Microstructural white matter changes in primary torsion dystonia. Mov. Disord. 23, 234–239. https://doi.org/10.1002/mds.21806.

Chen, C.H., Fremont, R., Arteaga-Bracho, E.E., Khodakhah, K., 2014. Short latency cerebellar modulation of the basal ganglia. Nat. Neurosci. 17, 1767–1775. https://doi.org/10.1038/nn.3868.

Chu, W.T., DeSimone, J.C., Riffe, C.J., Liu, H., Chakrabarty, P., Giasson, B.I., Vedam-Mai, V., Vaillancourt, D.E., 2020. Alpha-synuclein induces progressive changes in brain microstructure and sensory-evoked brain function that precedes locomotor decline. J. Neurosci. https://doi.org/10.1523/JNEUROSCI.0189-20.2020.

Coffman, K.A., Dum, R.P., Strick, P.L., 2011. Cerebellar vermis is a target of projections from the motor areas in the cerebral cortex. Proc. Natl. Acad. Sci. U. S. A. 108, 16068–16073. https://doi.org/10.1073/pnas.1107904108.

Colon-Perez, L.M., Ibanez, K.R., Suarez, M., Torroella, K., Acuna, K., Ofori, E., Levites, Y., Vaillancourt, D.E., Golde, T.E., Chakrabarty, P., Febo, M., 2019. Neurite orientation dispersion and density imaging reveals white matter and hippocampal microstructure changes produced by Interleukin-6 in the TgCRND8 mouse model of amyloidosis. Neuroimage 202, 116138. https://doi.org/10.1016/j.neuroimage.2019.116138.

Conte, A., McGovern, E.M., Narasimham, S., Beck, R., Killian, O., O'Riordan, S., Reilly, R. B., Hutchinson, M., 2017. Temporal discrimination: mechanisms and relevance to adult-onset dystonia. Front. Neurol. 8, 625. https://doi.org/10.3389/fneur.2017.00625.

Conte, A., Defazio, G., Hallett, M., Fabbrini, G., Berardelli, A., 2019. The role of sensory information in the pathophysiology of focal dystonias. Nat. Rev. Neurol. 15, 224–233. https://doi.org/10.1038/s41582-019-0137-9.

Cox, R.W., 1996. AFNI: software for analysis and visualization of functional magnetic resonance neuroimages. Comput. Biomed. Res. 29, 162–173. https://doi.org/10.1006/cbmr.1996.0014.

Cox, R.W., Chen, G., Glen, D.R., Reynolds, R.C., Taylor, P.A., 2017. fMRI clustering and false-positive rates. Proc. Natl. Acad. Sci. U. S. A. 114, E3370–E3371. https://doi.org/10.1073/pnas.1614961114.

Dang, M.T., Yokoi, F., McNaught, K., Jengelley, T.-A., Jackson, T., Li, J., Li, Y., 2005. Generation and characterization of Dyt1 ΔGAG knock-in mouse as a model for early-onset dystonia. Exp. Neurol. 196, 452–463. https://doi.org/10.1016/j.expneurol.2005.08.025.

Dang, M.T., Yokoi, F., Cheetham, C.C., Lu, J., Vo, V., Lovinger, D.M., Li, Y., 2012. An anticholinergic reverses motor control and corticostriatal LTD deficits in Dyt1 ΔGAG knock-in mice. Behav. Brain Res. 226, 465–472. https://doi.org/10.1016/j.bbr.2011.10.002.

DeAndrade, M.P., Trongnetrpunya, A., Yokoi, F., Cheetham, C.C., Peng, N., Wyss, J.M., Ding, M., Li, Y., 2016. Electromyographic evidence in support of a knock-in mouse model of DYT1 dystonia: EMG of a DYT1 dystonia mouse. Mov. Disord. 31, 1633–1639. https://doi.org/10.1002/mds.26677.

DeSimone, J.C., Febo, M., Shukla, P., Ofori, E., Colon-Perez, L.M., Li, Y., Vaillancourt, D. E., 2016. In vivo imaging reveals impaired connectivity across cortical and subcortical networks in a mouse model of DYT1 dystonia. Neurobiol. Dis. 95, 35–45. https://doi.org/10.1016/j.nbd.2016.07.005.

DeSimone, J.C., Pappas, S.S., Febo, M., Burciu, R.G., Shukla, P., Colon-Perez, L.M., Dauer, W.T., Vaillancourt, D.E., 2017. Forebrain knock-out of torsinA reduces striatal free-water and impairs whole-brain functional connectivity in a symptomatic mouse model of DYT1 dystonia. Neurobiol. Dis. 106, 124–132. https://doi.org/10.1016/j.nbd.2017.06.015.

Fahn, S., 1983. High dosage anticholinergic therapy in dystonia. Neurology 33, 1255–1261. https://doi.org/10.1212/wnl.33.10.1255.
Fiorio, M., Gambarin, M., Valente, E.M., Liberini, P., Loi, M., Cossu, G., Moretto, G., Bhatia, K.P., Defazio, G., Aglioti, S.M., Fiaschi, A., Tinazzi, M., 2007. Defective temporal processing of sensory stimuli in DYT1 mutation carriers: a new endophenotype of dystonia? Brain 130, 134–142. https://doi.org/10.1093/brain/awl283.
Fremont, R., Tewari, A., Angueyra, C., Khodakhah, K., 2017. A role for cerebellum in the hereditary dystonia DYT1. eLife 6. https://doi.org/10.7554/eLife.22775.
Garyfallidis, E., Brett, M., Amirbekian, B., Rokem, A., van der Walt, S., Descoteaux, M., Nimmo-Smith, I., Contributors, Dipy, 2014. Dipy, a library for the analysis of diffusion MRI data. Front Neuroinform 8, 8. https://doi.org/10.3389/fninf.2014.00008.
Gong, S., Doughty, M., Harbaugh, C.R., Cummins, A., Hatten, M.E., Heintz, N., Gerfen, C. R., 2007. Targeting Cre recombinase to specific neuron populations with bacterial artificial chromosome constructs. J. Neurosci. 27, 9817–9823. https://doi.org/10.1523/JNEUROSCI.2707-07.2007.
Hallett, M., 1995. Is dystonia a sensory disorder? Ann. Neurol. 38, 139–140. https://doi.org/10.1002/ana.410380203.
Hayashi, M., Nagao, Y., Kimura, K., Hachimori, K., Nomura, Y., Segawa, M., 2008. Case of DYT1 dystonia (early-onset torsion dystonia) showing long-term focal dystonia in the arm. No To Hattatsu 40, 483–486.
Hedges, V.L., Ebner, T.J., Meisel, R.L., Mermelstein, P.G., 2012. The cerebellum as a target for estrogen action. Front. Neuroendocrinol. 33, 403–411. https://doi.org/10.1016/j.yfrne.2012.08.005.
Jenkinson, M., Beckmann, C.F., Behrens, T.E.J., Woolrich, M.W., Smith, S.M., 2012. FSL. Neuroimage 62, 782–790. https://doi.org/10.1016/j.neuroimage.2011.09.015.
Kim, J., Yao, A., Atherley, R., Carstens, E., Jinks, S.L., Antognini, J.F., 2007. Neurons in the ventral spinal cord are more depressed by isoflurane, halothane, and propofol than are neurons in the dorsal spinal cord. Anesth. Analg. 105, 1020–1026 table of contents. https://doi.org/10.1213/01.ane.0000280483.17854.56.
Koch, G., Porcacchia, P., Ponzo, V., Carrillo, F., Cáceres-Redondo, M.T., Brusa, L., Desiato, M.T., Arciprete, F., Di Lorenzo, F., Pisani, A., Caltagirone, C., Palomar, F.J., Mir, P., 2014. Effects of two weeks of cerebellar theta burst stimulation in cervical dystonia patients. Brain Stimul 7, 564–572. https://doi.org/10.1016/j.brs.2014.05.002.
Lee, A., Furuya, S., Altenmüller, E., 2014. Epidemiology and treatment of 23 musicians with task specific tremor. J Clin Mov Disord 1, 5. https://doi.org/10.1186/2054-7072-1-5.
Liu, Y., Xing, H., Wilkes, B.J., Yokoi, F., Chen, H., Vaillancourt, D.E., Li, Y., 2020. The abnormal firing of Purkinje cells in the knockin mouse model of DYT1 dystonia. Brain Res. Bull. 165, 14–22. https://doi.org/10.1016/j.brainresbull.2020.09.011.
Lyu, S., Xing, H., DeAndrade, M.P., Perez, P.D., Yokoi, F., Febo, M., Walters, A.S., Li, Y., 2020. The role of BTBD9 in the cerebellum, sleep-like behaviors and the restless legs syndrome. Neuroscience 440, 85–96. https://doi.org/10.1016/j.neuroscience.2020.05.021.
MacIver, C.L., Tax, C.M.W., Jones, D.K., Peall, K.J., 2022. Structural magnetic resonance imaging in dystonia: a systematic review of methodological approaches and findings. Eur. J. Neurol. 29, 3418–3448. https://doi.org/10.1111/ene.15483.
Maltese, M., Martella, G., Madeo, G., Fagiolo, I., Tassone, A., Ponterio, G., Sciamanna, G., Burbaud, P., Conn, P.J., Bonsi, P., Pisani, A., 2014. Anticholinergic drugs rescue synaptic plasticity in DYT1 dystonia: role of M1 muscarinic receptors. Mov. Disord. 29, 1655–1665. https://doi.org/10.1002/mds.26009.
Martella, G., Tassone, A., Sciamanna, G., Platania, P., Cuomo, D., Viscomi, M.T., Bonsi, P., Cacci, E., Biagioni, S., Usiello, A., Bernardi, G., Sharma, N., Standaert, D. G., Pisani, A., 2009. Impairment of bidirectional synaptic plasticity in the striatum of a mouse model of DYT1 dystonia: role of endogenous acetylcholine. Brain 132, 2336–2349. https://doi.org/10.1093/brain/awp194.
Martella, G., Maltese, M., Nisticò, R., Schirinzi, T., Madeo, G., Sciamanna, G., Ponterio, G., Tassone, A., Mandolesi, G., Vanni, V., Pignatelli, M., Bonsi, P., Pisani, A., 2014. Regional specificity of synaptic plasticity deficits in a knock-in mouse model of DYT1 dystonia. Neurobiol. Dis. 65, 124–132. https://doi.org/10.1016/j.nbd.2014.01.016.
Mazere, J., Dilharreguy, B., Catheline, G., Vidailhet, M., Deffains, M., Vimont, D., Ribot, B., Barse, E., Cif, L., Mazoyer, B., Langbour, N., Pisani, A., Allard, M., Lamare, F., Guehl, D., Fernandez, P., Burbaud, P., 2021. Striatal and cerebellar vesicular acetylcholine transporter expression is disrupted in human DYT1 dystonia. Brain 144, 909–923. https://doi.org/10.1093/brain/awaa465.
Meoni, S., Macerollo, A., Moro, E., 2020. Sex differences in movement disorders. Nat. Rev. Neurol. 16, 84–96. https://doi.org/10.1038/s41582-019-0294-x.
Miyazaki, Y., 2012. Efficacy of zolpidem for dystonia: a study among different subtypes. Front. Neuroendocrinol. 6 https://doi.org/10.3389/fneur.2012.00058.
Ozelius, L.J., Hewett, J.W., Page, C.E., Bressman, S.B., Kramer, P.L., Shalish, C., de Leon, D., Brin, M.F., Raymond, D., Corey, D.P., Fahn, S., Risch, N.J., Buckler, A.J., Gusella, J.F., Breakefield, X.O., 1997. The early-onset torsion dystonia gene (DYT1) encodes an ATP-binding protein. Nat. Genet. 17, 40–48. https://doi.org/10.1038/ng0997-40.
Pisano, T.J., Dhanerawala, Z.M., Kislin, M., Bakshinskaya, D., Engel, E.A., Hansen, E.J., Hoag, A.T., Lee, J., de Oude, N.L., Venkataraju, K.U., Verpeut, J.L., Hoebeek, F.E., Richardson, B.D., Boele, H.-J., Wang, S.S.-H., 2021. Homologous organization of cerebellar pathways to sensory, motor, and associative forebrain. Cell Rep. 36, 109721 https://doi.org/10.1016/j.celrep.2021.109721.
Premi, E., Diano, M., Gazzina, S., Cauda, F., Gualeni, V., Tinazzi, M., Fiorio, M., Liberini, P., Lazzarini, C., Archetti, S., Biasiotto, G., Turla, M., Bertasi, V., Cotelli, M., Gasparotti, R., Padovani, A., Borroni, B., 2016. Functional connectivity networks in asymptomatic and symptomatic DYT1 carriers. Mov. Disord. 31, 1739–1743. https://doi.org/10.1002/mds.26725.
Quartarone, A., Hallett, M., 2013. Emerging concepts in the physiological basis of dystonia. Mov. Disord. 28, 958–967. https://doi.org/10.1002/mds.25532.
Raz, N., Gunning-Dixon, F., Head, D., Williamson, A., Acker, J.D., 2001. Age and sex differences in the cerebellum and the ventral pons: a prospective MR study of healthy adults. AJNR Am. J. Neuroradiol. 22, 1161–1167.
Rijpkema, M., Everaerd, D., van der Pol, C., Franke, B., Tendolkar, I., Fernández, G., 2012. Normal sexual dimorphism in the human basal ganglia. Hum. Brain Mapp. 33, 1246–1252. https://doi.org/10.1002/hbm.21283.
Rottmann, S., Jung, K., Vohn, R., Ellrich, J., 2010. Long-term depression of pain-related cerebral activation in healthy man: an fMRI study. Eur. J. Pain 14, 615–624. https://doi.org/10.1016/j.ejpain.2009.10.006.
Saad, Z.S., Chen, G., Reynolds, R.C., Christidis, P.P., Hammett, K.R., Bellgowan, P.S.F., Cox, R.W., 2006. Functional imaging analysis contest (FIAC) analysis according to AFNI and SUMA. Hum. Brain Mapp. 27, 417–424. https://doi.org/10.1002/hbm.20247.
Satterthwaite, T.D., Elliott, M.A., Gerraty, R.T., Ruparel, K., Loughead, J., Calkins, M.E., Eickhoff, S.B., Hakonarson, H., Gur, R.C., Gur, R.E., Wolf, D.H., 2013. An improved framework for confound regression and filtering for control of motion artifact in the preprocessing of resting-state functional connectivity data. Neuroimage 64, 240–256. https://doi.org/10.1016/j.neuroimage.2012.08.052.
Scuteri, D., Rombolà, L., Natoli, S., Pisani, A., Bonsi, P., Hamamura, K., Bagetta, G., Tonin, P., Corasaniti, M.T., 2021. Exploitation of thermal sensitivity and hyperalgesia in a mouse model of dystonia. Life (Basel) 11, 985. https://doi.org/10.3390/life11090985.
Sharma, N., Baxter, M.G., Petravicz, J., Bragg, D.C., Schienda, A., Standaert, D.G., Breakefield, X.O., 2005. Impaired motor learning in mice expressing torsinA with the DYT1 dystonia mutation. J. Neurosci. 25, 5351–5355. https://doi.org/10.1523/JNEUROSCI.0855-05.2005.
Shashidharan, P., Sandu, D., Potla, U., Armata, I.A., Walker, R.H., McNaught, K.S., Weisz, D., Sreenath, T., Brin, M.F., Olanow, C.W., 2005. Transgenic mouse model of early-onset DYT1 dystonia. Hum. Mol. Genet. 14, 125–133. https://doi.org/10.1093/hmg/ddi012.
Simonyan, K., 2018. Neuroimaging applications in dystonia. Int. Rev. Neurobiol. 143, 1–30. https://doi.org/10.1016/bs.irn.2018.09.007.
Song, C.-H., Bernhard, D., Bolarinwa, C., Hess, E.J., Smith, Y., Jinnah, H.A., 2013. Subtle microstructural changes of the striatum in a DYT1 knock-in mouse model of dystonia. Neurobiol. Dis. 54, 362–371. https://doi.org/10.1016/j.nbd.2013.01.008.
Song, C.-H., Bernhard, D., Hess, E.J., Jinnah, H.A., 2014. Subtle microstructural changes of the cerebellum in a knock-in mouse model of DYT1 dystonia. Neurobiol. Dis. 62, 372–380. https://doi.org/10.1016/j.nbd.2013.10.003.
Suttrup, I., Oberdiek, D., Suttrup, J., Osada, N., Evers, S., Marziniak, M., 2011. Loss of sensory function in patients with idiopathic hand dystonia. Mov. Disord. 26, 107–113. https://doi.org/10.1002/mds.23425.
Tewari, A., Fremont, R., Khodakhah, K., 2017. It's not just the basal ganglia: cerebellum as a target for dystonia therapeutics. Mov. Disord. 32, 1537–1545. https://doi.org/10.1002/mds.27123.
Tinazzi, M., Rosso, T., Fiaschi, A., 2003. Role of the somatosensory system in primary dystonia. Mov. Disord. 18, 605–622. https://doi.org/10.1002/mds.10398.
Uluğ, A.M., Vo, A., Argyelan, M., Tanabe, L., Schiffer, W.K., Dewey, S., Dauer, W.T., Eidelberg, D., 2011. Cerebellothalamocortical pathway abnormalities in torsinA DYT1 knock-in mice. Proc. Natl. Acad. Sci. U. S. A. 108, 6638–6643. https://doi.org/10.1073/pnas.1016445108.
Vo, A., Sako, W., Dewey, S.L., Eidelberg, D., Uluğ, A.M., 2015a. 18FDG-microPET and MR DTI findings in Tor1a+/− heterozygous knock-out mice. Neurobiol. Dis. 73, 399–406. https://doi.org/10.1016/j.nbd.2014.10.020.
Vo, A., Sako, W., Niethammer, M., Carbon, M., Bressman, S.B., Uluğ, A.M., Eidelberg, D., 2015b. Thalamocortical connectivity correlates with phenotypic variability in dystonia. Cereb. Cortex 25, 3086–3094. https://doi.org/10.1093/cercor/bhu104.
Wilkes, B.J., DeSimone, J.C., Liu, Y., Chu, W.T., Coombes, S.A., Li, Y., Vaillancourt, D.E., 2021. Cell-specific effects of Dyt1 knock-out on sensory processing, network-level connectivity, and motor deficits. Exp. Neurol. 343, 113783 https://doi.org/10.1016/j.expneurol.2021.113783.
Xing, H., Yokoi, F., Walker, A.L., Torres-Medina, R., Liu, Y., Li, Y., 2022. Electrophysiological characterization of the striatal cholinergic interneurons in Dyt1 ΔGAG knock-in mice. Dystonia 1, 10557. https://doi.org/10.3389/dyst.2022.10557.
Yokoi, F., Dang, M.T., Li, Y., 2012. Improved motor performance in Dyt1 ΔGAG heterozygous knock-in mice by cerebellar Purkinje-cell specific Dyt1 conditional knocking-out. Behav. Brain Res. 230, 389–398. https://doi.org/10.1016/j.bbr.2012.02.029.
Yokoi, F., Oleas, J., Xing, H., Liu, Y., Dexter, K.M., Misztal, C., Gerard, M., Efimenko, I., Lynch, P., Villanueva, M., Alsina, R., Krishnaswamy, S., Vaillancourt, D.E., Li, Y., 2020. Decreased number of striatal cholinergic interneurons and motor deficits in dopamine receptor 2-expressing-cell-specific Dyt1 conditional knockout mice. Neurobiol. Dis. 134, 104638 https://doi.org/10.1016/j.nbd.2019.104638.
Zhang, L., Yokoi, F., Jin, Y.-H., DeAndrade, M.P., Hashimoto, K., Standaert, D.G., Li, Y., 2011. Altered dendritic morphology of Purkinje cells in Dyt1 ΔGAG knock-in and purkinje cell-specific Dyt1 conditional knockout mice. PLoS One 6, e18357. https://doi.org/10.1371/journal.pone.0018357.